

# Undergraduate setup for measuring the Bell inequalities and performing Quantum State Tomography

Raul Lahoz Sanz,<sup>1,2,\*</sup> Lidia Lozano Martín,<sup>2,3</sup> Adrià Brú i Cortés,<sup>4,2</sup>  
Martí Duocastella,<sup>3,5</sup> Jose M. Gómez Cama,<sup>4,2,6</sup> and Bruno Juliá-Díaz<sup>1,2</sup>

<sup>1</sup>*Departament de Física Quàntica i Astrofísica,  
Facultat de Física, Universitat de Barcelona (QCommsUB group)*

<sup>2</sup>*Institut de Ciències del Cosmos (ICCUB), Universitat de Barcelona (UB),  
c. Martí i Franqués, 1, 08028 Barcelona, Spain*

<sup>3</sup>*Department of Applied Physics, Universitat de Barcelona, C/Martí i Franqués 1, 08028, Barcelona, Spain*

<sup>4</sup>*Departament d'Enginyeria Electrònica i Biomèdica,  
Universitat de Barcelona (UB), c. Martí i Franqués, 1, 08028 Barcelona, Spain*

<sup>5</sup>*Institute of Nanoscience and Nanotechnology (IN2UB),  
Universitat de Barcelona (UB), 08028, Barcelona, Spain*

<sup>6</sup>*Institut d'Estudis Espacials de Catalunya (IEEC), Edifici RDIT,  
Campus UPC, 08860 Castelldefels (Barcelona), Spain*

The growth of quantum technologies is attracting the interest of many students eager to learn concepts such as quantum entanglement or quantum superposition. However, the non-intuitive nature of these concepts poses a challenge to understanding them. Here, we present an entangled photon system which can perform a Bell test, i.e. the CHSH inequality, and can obtain the complete tomography of the two-photon state. The proposed setup is versatile, cost-effective and allows for multiple classroom operating modes. We present two variants, both facilitating the measurement of Bell inequalities and quantum state tomography. Experimental results showcase successful manipulation of the quantum state of the photons, achieving high-fidelity entangled states and significant violations of Bell's inequalities. Our setup's simplicity and affordability enhances accessibility for less specialized laboratories, allowing students to familiarize themselves with quantum physics concepts.

## I. INTRODUCTION

Quantum superposition and entanglement are key elements in the current developments in quantum technologies [1]. However, they are elusive concepts with no classical counterpart, making them difficult to understand for undergraduate students and non-quantum experts. An important step to close this gap is through hands on experimentation. By acquiring and analyzing data from a quantum entanglement setup, students can get acquainted with quantum mechanical concepts and grasp the non-intuitive nature of quantum physics. Still, a comprehensive description of such a system, which is easily accessible for undergraduate students and suitable to generate quality data within the time frame of lab practises (a couple of hours), remains difficult to find.

Quantum entanglement, the phenomenon by which two particles become linked so that the state of one affects the state of another, regardless of distance, is central in today's quantum technologies. Examples include quantum computation, e.g. see Shor's algorithm [2], quantum sensing, e.g. enhancing the LIGO detecting capability [3], and quantum communications, see the Ekert91 protocol [4]. Despite its importance, quantum entanglement has been controversial since the well known EPR paper [5]. There, Einstein, Podolsky and Rosen argued that the quantum mechanical description of a seemingly simple system composed of two particles was most

likely incomplete. They introduced the notion of hidden variables, which at the time seemed more of a philosophical idea than an empirically testable one, that would make the description of nature complete.

The situation changed drastically thanks to Bell's article in 1964 [6]. There, he found a way of experimentally setting bounds to the existence of hidden variables. He proposed specific experiments to prove quantum mechanical predictions could not be explained with hidden variables. Since then, numerous experiments have been conducted to verify his predictions. From the pioneering experiment by John F. Clauser and Stuart Freedman [7] onward, all have supported the Copenhagen interpretation, emphasizing the intrinsic randomness of nature and ruling out the possibility of including hidden variables in the theory [8–10]. The importance of these results was clearly stated by the Nobel prize in Physics in 2022, awarded to Alain Aspect, John F. Clauser and Anton Zeilinger “for experiments with entangled photons, establishing the violation of Bell inequalities and pioneering quantum information science” [11].

In the last two decades, numerous efforts have been made to render this type of experiment accessible to undergraduate students. In the universities where these laboratory setups have been implemented, e.g. [12–17], there has been a notable improvement in understanding concepts pertaining to quantum physics, along with a considerable higher enthusiasm among students for such technologies [18, 19].

The main goal of this paper is to present an experimental setup for undergraduate students that allows a

\* rlahozsanz@icc.ub.edu

thorough study of the Bell inequalities. For this purpose, we describe the implementation, operation and alignment of two such setups, enabling students to build them from scratch. Thus, our detailed guidelines offer students a pathway to their first hands-on experience with quantum concepts.

We see a clear pedagogical value in our work, which can be at least twofold: reproducing the experiment can be embedded in the syllabus as a final degree project for one or two students. Once built, the proposed setup can serve as an advanced quantum system in experimental laboratories, in our case it is part of the Advanced Quantum Laboratory of the Master in Quantum Science and Technology in Barcelona.

To provide a concise yet self contained document, we describe the essential theoretical formalism needed to understand the experiment followed by a detailed description of the practical setup implementation. The article is organized as follows. First, in Sec. II we present the main theoretical concepts involved, including the suitable basis states to describe the two-photon states and how to perform operations on them. This section also provides a theoretical description of the quantum state tomography (QST), necessary to fully reconstruct the state (subsection II B). We then introduce Bell inequalities, particularly the CHSH inequality [20] (subsection II D). The experimental setups are described in Sec. III, providing comprehensive descriptions of the proposed implementation. Subsections III A and III B explain the production and measurement of photons in the two respective schemes. The way to align and run the experiment is shown in Sec. IV while the experimental results are collected in Sec. V. Finally, in Sec. VI, we outline the qualities of our setups and the results of our experiments. We also discuss how this work can help to bring these types of concepts and technologies closer to a broader and less specialized audience.

## II. THEORY

In this section we provide the basic theoretical tools needed to understand the proposed experiments.

### A. Definition of states and operators

As the photon is the quantum system of our experiments, we start by defining its quantum state. It can be described in several useful basis. The most common, the canonical basis  $\{|H\rangle, |V\rangle\}$  is formed by the vectors,

$$|H\rangle = \begin{pmatrix} 1 \\ 0 \end{pmatrix} \quad \text{and} \quad |V\rangle = \begin{pmatrix} 0 \\ 1 \end{pmatrix}. \quad (1)$$

A set of of different basis, relevant for the experiment described herein, are the Diagonal and Antidiagonal basis, the Right-handed and Left-handed basis, and the  $\alpha$

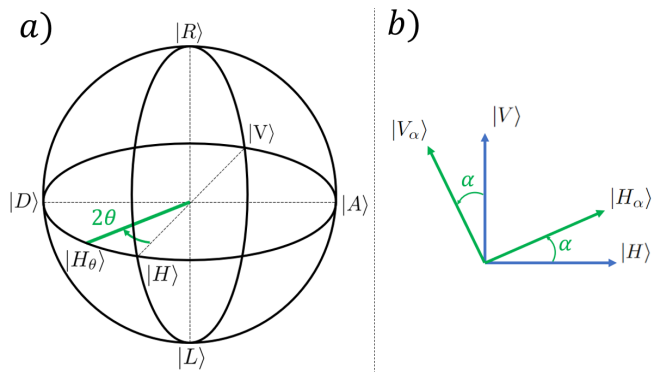


FIG. 1. a) Visual representation of the Bloch sphere. All possible states of one single qubit are contained in the surface of the sphere. b) Representation of the  $\{|H\rangle, |V\rangle\}$  and  $\{|H_\alpha\rangle, |V_\alpha\rangle\}$  basis. The equator of the Bloch sphere is the circle generated by the  $\{|H_\alpha\rangle, |V_\alpha\rangle\}$  states.

rotated basis. Note that, in this description, photons consist of a two-level quantum mechanical system, known as a qubit in the quantum information community. Expressed in terms of  $\{|H\rangle, |V\rangle\}$ , these basis can be written as

$$\{|D\rangle, |A\rangle\} = \left\{ \frac{1}{\sqrt{2}} \begin{pmatrix} 1 \\ 1 \end{pmatrix}, \frac{1}{\sqrt{2}} \begin{pmatrix} 1 \\ -1 \end{pmatrix} \right\}, \quad (2)$$

$$\{|R\rangle, |L\rangle\} = \left\{ \frac{1}{\sqrt{2}} \begin{pmatrix} 1 \\ -i \end{pmatrix}, \frac{1}{\sqrt{2}} \begin{pmatrix} 1 \\ i \end{pmatrix} \right\}, \quad (3)$$

$$\{|H_\alpha\rangle, |V_\alpha\rangle\} = \left\{ \begin{pmatrix} \cos \alpha \\ \sin \alpha \end{pmatrix}, \begin{pmatrix} -\sin \alpha \\ \cos \alpha \end{pmatrix} \right\}. \quad (4)$$

Where we define the counterclockwise direction  $\alpha$  as positive when we observe the light moving away from us. Thus, in Fig. 1 b), the light propagates towards the interior of the paper.

The way to perform unitary operations on quantum states without measuring them is using retarder plates, particularly half-wave plates (HWP) and quarter-wave plates (QWP). As these operations are important in our setup, we provide a formal definition of their actions in the  $\{|H\rangle, |V\rangle\}$  basis. The action of a HWP and a QWP with their fast axis set at an angle  $\theta$  w.r.t the horizontal, i.e. the fast axis pointing at the direction  $|H_\theta\rangle$ , is described by

$$\text{HWP}_\theta = e^{-i\frac{\pi}{2}} \begin{pmatrix} \cos 2\theta & \sin 2\theta \\ \sin 2\theta & -\cos 2\theta \end{pmatrix},$$

$$\text{QWP}_\theta = e^{-i\frac{\pi}{4}} \begin{pmatrix} \cos^2 \theta + i \sin^2 \theta & (1-i) \sin \theta \cos \theta \\ (1-i) \sin \theta \cos \theta & \sin^2 \theta + i \cos^2 \theta \end{pmatrix}.$$

Importantly, all these operations can be represented in the Bloch sphere, as shown in Fig. 1 a) [21]. A HWP (QWP) with its fast axis set at an angle defined by the vector  $|H_\theta\rangle$ , performs rotations of  $180^\circ$  ( $90^\circ$ ) of any single photon state with respect to the axis defined by the direction of the fast axis.

## B. Reconstruction of a general two-photon state. Quantum State Tomography

The next step is to introduce two-photon states, which represent the minimal photonic system which can exhibit quantum entanglement. As customary in quantum optics and quantum information, we name Alice and Bob the two individuals that measure the first and the second photon, respectively.

The general case of non-pure two-photon states can be fully described by the density matrix. In other words, by experimentally measuring the density matrix, one can gather all the necessary information to assess two-photon states, a process known as quantum state tomography. The density matrix can be written as,

$$\hat{\rho} = \begin{pmatrix} A_1 & B_1 e^{i\phi_1} & B_2 e^{i\phi_2} & B_3 e^{i\phi_3} \\ B_1 e^{-i\phi_1} & A_2 & B_4 e^{i\phi_4} & B_5 e^{i\phi_5} \\ B_2 e^{-i\phi_2} & B_4 e^{-i\phi_4} & A_3 & B_6 e^{i\phi_6} \\ B_3 e^{-i\phi_3} & B_5 e^{-i\phi_5} & B_6 e^{-i\phi_6} & A_4 \end{pmatrix}, \quad (5)$$

where the basis used is  $\{|HH\rangle, |HV\rangle, |VH\rangle, |VV\rangle\}$ . Note that this matrix is hermitian  $\rho = \rho^\dagger$  and thus semi-definite positive. Also, the trace has to be equal to 1, i.e.  $A_1 + A_2 + A_3 + A_4 = 1$ . Thus, we need  $16 - 1 = 15$  parameters to fully characterize the matrix. For our experiments, it is useful to expand the density matrix as a sum of tensor products of two Pauli matrices, see for instance [21],

$$\hat{\rho} = \frac{1}{4} \sum_{i,j=0}^3 S_{ij} \cdot \hat{\sigma}_i \otimes \hat{\sigma}_j, \quad (6)$$

where  $\hat{\sigma}_i$  are the identity and the usual Pauli matrices defined as

$$\begin{aligned} \hat{\sigma}_0 &= |V\rangle\langle V| + |H\rangle\langle H| = \begin{pmatrix} 1 & 0 \\ 0 & 1 \end{pmatrix}, \\ \hat{\sigma}_1 &= |D\rangle\langle D| - |A\rangle\langle A| = \begin{pmatrix} 0 & 1 \\ 1 & 0 \end{pmatrix}, \\ \hat{\sigma}_2 &= |L\rangle\langle L| - |R\rangle\langle R| = \begin{pmatrix} 0 & -i \\ i & 0 \end{pmatrix}, \\ \hat{\sigma}_3 &= |H\rangle\langle H| - |V\rangle\langle V| = \begin{pmatrix} 1 & 0 \\ 0 & -1 \end{pmatrix}. \end{aligned}$$

Importantly, the coefficients defining the state,  $S_{ij}$  in Eq. (6), named Stokes coefficients, can be obtained from combined experimental measurements of the two photons in the state. For instance,

$$S_{00} = P_{|HH\rangle} + P_{|HV\rangle} + P_{|VH\rangle} + P_{|VV\rangle}, \quad (7)$$

where  $P_{|\sigma\sigma'\rangle}$  is the joint probability that Alice and Bob have of obtaining their respective photons in the states  $|\sigma\rangle$  and  $|\sigma'\rangle$  when Alice is measuring in the basis  $\{|\sigma\rangle, |\sigma^\perp\rangle\}$  and Bob in the basis  $\{|\sigma'\rangle, |\sigma'^\perp\rangle\}$ . The explicit expressions for all Stokes coefficients can be found

in Appendix B. This forms the basis of quantum state tomography.

In our experiment we produce two-photon states which are pure states. They are a particular case of the general one in Eq. (5), and can be written as

$$|\Psi\rangle = a_0 |HH\rangle + a_1 |HV\rangle + a_2 |VH\rangle + a_3 |VV\rangle, \quad (8)$$

with  $a_i$  ( $i = 0, 1, 2, 3$ ) complex coefficients such that  $\sum_{i=0}^3 |a_i|^2 = 1$ .

To compare how similar are two distinct two-photon states,  $\hat{\rho}_1$  and  $\hat{\rho}_2$ , we define the fidelity,  $F(\hat{\rho}_1, \hat{\rho}_2)$ , [22],

$$F(\hat{\rho}_1, \hat{\rho}_2) = \left( \text{Tr} \left[ \sqrt{\sqrt{\hat{\rho}_1} \hat{\rho}_2 \sqrt{\hat{\rho}_1}} \right] \right)^2. \quad (9)$$

Furthermore, if one of the two states under comparison is pure ( $\hat{\rho}_2 = |\Psi_2\rangle\langle\Psi_2|$ ), the expression defined in Eq. (9) becomes

$$F(\hat{\rho}_1, \hat{\rho}_2) = \text{Tr}(\hat{\rho}_1 |\Psi_2\rangle\langle\Psi_2|) = \langle\Psi_2| \hat{\rho}_1 |\Psi_2\rangle. \quad (10)$$

The values of the fidelity fall between 0 and 1. Fidelity 1 is only achieved if both states are equal, while fidelity 0 is obtained for orthogonal states.

## C. Entangled States

A key concept for this work is that of quantum entanglement. Working with pure states of the form of Eq. (8), a two-photon state is said to be entangled if it cannot be written as a separable state,

$$|\Psi\rangle_{\text{Separable}} = |\psi\rangle \otimes |\varphi\rangle. \quad (11)$$

with  $|\psi\rangle$  and  $|\varphi\rangle$  single photon states. Note that in a separable state, the outcomes of the measurements of Alice and Bob are completely independent, while in entangled states, quantum correlations arise between the two outcomes.

A set of well-known and useful entangled states are the so-called Bell states,

$$\begin{aligned} |\Phi^+\rangle &= \frac{1}{\sqrt{2}}(|HH\rangle + |VV\rangle), \\ |\Phi^-\rangle &= \frac{1}{\sqrt{2}}(|HH\rangle - |VV\rangle), \\ |\Psi^+\rangle &= \frac{1}{\sqrt{2}}(|HV\rangle + |VH\rangle), \\ |\Psi^-\rangle &= \frac{1}{\sqrt{2}}(|HV\rangle - |VH\rangle). \end{aligned}$$

These states, in turn, form a basis of the two-photon Hilbert space.

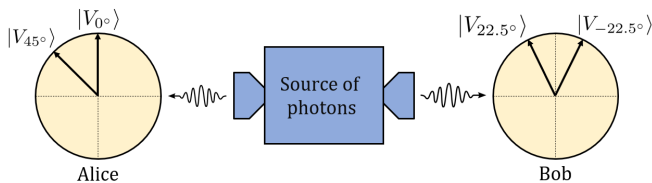


FIG. 2. Sketch of the CHSH protocol: A source generates photon pairs always in the same state, sending one to Alice and the other to Bob. They can determine if the received pairs are entangled performing measurements in different bases and sharing their results.

#### D. Bell Test - CHSH inequality

The correlations stemming from the non-separability of states rose important criticism. Notably, in the so-called EPR paradox stated in Ref. [5], it was argued that the description of nature is probably incomplete, calling for the existence of so-called hidden variables. John Bell [6] introduced the first empirical approach to distinguish predictions from hidden variable theories. Since then, a series of Bell-type inequalities, i.e. Bell tests, have been developed to check if the quantum state associated to two particles follows a non-local behaviour. In particular, quantum mechanics produces predictions which violate Bell inequalities, i.e. they are incompatible with hidden variable theories. In our case, we consider the CHSH inequality [20], which was the one used by the pioneering article of Aspect and collaborators [8], and also in the pedagogical setup of Ref.-[23].

To carry out the Bell test, we consider the scenario described in Fig. 2. There, a source generates pairs of photons, named signal and idler, that are always produced in the same manner, and thus in the same quantum state, and that are sent in different directions. The receivers of these photons, again Alice and Bob, can determine whether the pairs of photons they share are entangled or not by performing measurements of the individual photons separately and communicating the results.

We define the functions  $a(\alpha)$  ( $b(\beta)$ ) as  $a(\alpha) = 1$  ( $b(\beta) = 1$ ) if Alice (Bob) measures the signal (idler) photon in the state  $|V_\alpha\rangle$  and  $a(\alpha) = -1$  ( $b(\beta) = -1$ ) if Alice (Bob) measures the signal (idler) photon in the state  $|H_\alpha\rangle$ . Then, we define the correlation function  $E(\alpha, \beta)$ , i.e. the average of the product of both measurements, as

$$E(\alpha, \beta) = \langle a(\alpha) \cdot b(\beta) \rangle = P_{|V_\alpha V_\beta\rangle} - P_{|V_\alpha H_\beta\rangle} - P_{|H_\alpha V_\beta\rangle} + P_{|H_\alpha H_\beta\rangle}. \quad (12)$$

In the CHSH inequality, Alice (Bob) measures the state of the photons in two different states,  $\alpha = 0^\circ$  ( $\beta = 22.5^\circ$ ) and  $\alpha' = 45^\circ$  ( $\beta' = -22.5^\circ$ ). Thus, Alice and Bob obtain four different values of Eq. (12), one for each combination of angles.  $E(\alpha, \beta)$ ,  $E(\alpha', \beta)$ ,  $E(\alpha, \beta')$  and  $E(\alpha', \beta')$ . Using these four values, we define the functions  $S$  and  $S'$  as,

$$S = E(\alpha, \beta) + E(\alpha, \beta') + E(\alpha', \beta) - E(\alpha', \beta'), \quad (13)$$

$$S' = E(\alpha, \beta) + E(\alpha, \beta') - E(\alpha', \beta) + E(\alpha', \beta'). \quad (14)$$

These functions are constructed to always yield a value between  $-2$  and  $+2$  when working with classical correlations, including the case of variables hidden theories. In contrast, their value falls between  $-2\sqrt{2}$  and  $+2\sqrt{2}$  when we compute the averages with quantum mechanics. Specifically, for each Bell state, one of them yields a result of zero, while the other provides a value equal to  $-2\sqrt{2}$  or  $+2\sqrt{2}$ :

- If the two photons are in the state  $|\Phi^{+(-)}\rangle$  we obtain  $\langle S \rangle = 2\sqrt{2}(0)$  and  $\langle S' \rangle = 0(2\sqrt{2})$ .
- If the two photons are in the state  $|\Psi^{+(-)}\rangle$  we obtain  $\langle S \rangle = 0(-2\sqrt{2})$  and  $\langle S' \rangle = -2\sqrt{2}(0)$ .

The fact that different Bell states require different Bell test functions  $S$  and  $S'$  is often not emphasized. In our case, we can precisely control the relative phase between components in the wave function of photon pairs along with the use of a HWP in one of the photons' paths. Thus, with our setups, we have the ability to generate the four maximally entangled Bell states, as is described later in Sec. III A. This two features set our work apart from other pedagogical setups.

### III. EXPERIMENTAL SETUPS

The two setups presented herein consist of a photon pair production part followed by a photon detection part. They both enable performing a full two-photon state tomography and a Bell test, and incorporate improvements at both the technical and conceptual level with respect to previous works. Among them, our setups allow us to prepare different Bell states, which emphasizes the fact that Bell tests are tailored for specific states. Also, both options feature a significantly simpler optical alignment of the elements of the setup and are fairly robust. Importantly, the measurement time is very reasonable: a Bell test can be performed in less than one hour, providing ample options for lab experimentation at both the graduate and master level.

A detailed list of the necessary equipment for each setup is compiled in Appendix A. The main difference between the two setups lies in the photon detection process. The first setup, illustrated in Fig. 3, employs only two inputs of the 4-channel detector (SPCM-AQ4C, Excelitas Technologies) and measures the polarization of the light using a QWP and a polarizer. While simpler in terms of optical elements, this option is slower for measurements. It can only provide the number of coincident photon counts passing through both polarizers in a single measurement. That is, pairs of photons that pass through both polarizers without being stopped and are detected simultaneously. The second setup, depicted in Fig. 4, needs all 4 inputs of the detector and directs photons to different detectors based on their polarization using polarizing beam splitters (PBS). Although this option

requires more optical elements, it is faster for measurements as it allows for the measurement of photon counts in any of the states of a given basis in a single measurement.

In both of our setups, as in some other pedagogical experiments [13, 14, 17], collimating lenses (F810FC-780, ThorLabs) and optical fibers are used to capture photons. This offers a significant advantage in alignment as is discussed in Sect. IV A. In some previous works [12, 23, 24] the alignment of the system and the capture of photons was performed without the use of optical fibers. To count coincidences between two channels we have replicated the circuit described in Ref. [24] modifying the capacitors to reduce the coincidence window to 90 ns and adding USB connectivity.

### A. Photon Production

As shown in Fig. 3 and Fig. 4, the two-photon production part is similar in both setups. It also shares many elements with previous works, in particular with that of Dehlinger and Mitchell [23, 24]. In more detail, we use a 405nm laser beam (L404P400M, ThorLabs) working at 400mW that emits light horizontally-polarized

$$|\Psi\rangle = |H\rangle_{\text{Pump}}.$$

To switch from horizontal to diagonal light with almost no energy loss, we employ a HWP with its optical axis set at an angle  $\theta = 22.5^\circ$

$$\text{HWP}_{\theta=22.5^\circ}^{(1)} |H\rangle = e^{i\frac{\pi}{2}} |D\rangle = |D\rangle.$$

Additionally, we place a polarizer set at an angle of  $45^\circ$  to further ensure the desired polarization state. Thus, the quantum state after the polarizer reads,

$$|\Psi\rangle = |D\rangle_{\text{Pump}}.$$

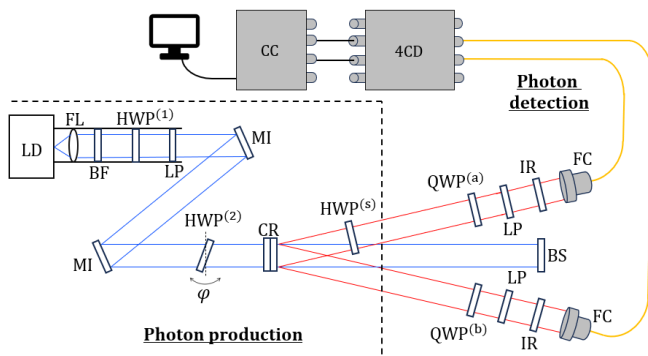


FIG. 3. Scheme setup 1. LD. laser diode, FL. focusing lens, BF. blue filter, LP. linear polarizer, MI. mirror, CR. BBO crystals, HWP. half-wave plate, QWP. quarter-wave plate, IR. infrared filter, FC. fiber-coupler lenses, 4CD. 4-channel detector, CC. Coincidence Circuit.

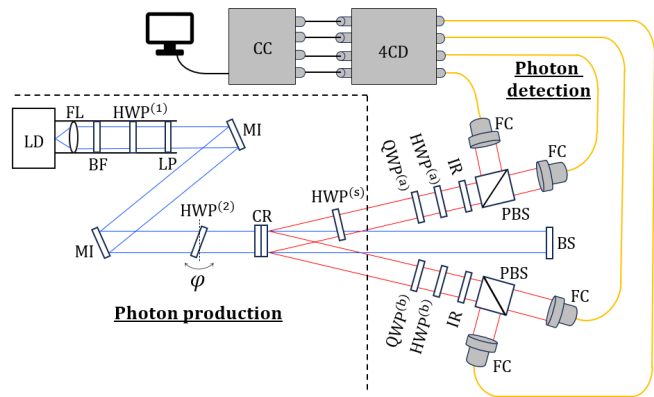


FIG. 4. Scheme setup 2. PBS. polarizing beam splitter. The rest of the elements are labeled in the same way as in Fig. 3.

Afterwards, the light gets reflected by the two 3D-precision mirrors and passes through a HWP with its fast axis parallel to the optical table. This HWP is mounted on a goniometer (RP01/M, ThorLabs) that allows us to tilt it around the axis perpendicular to the optical table. With this tilt angle  $\varphi$  we can vary the relative phase ( $\phi(\varphi)$ ) between the  $|H\rangle$  and  $|V\rangle$  component.

$$|\Psi\rangle = \frac{1}{\sqrt{2}} \left( |H\rangle_{\text{Pump}} + e^{i\phi(\varphi)} |V\rangle_{\text{Pump}} \right). \quad (15)$$

Note that, at this stage, we have produced a photon in a superposition of both horizontal and vertical polarization. To generate entangled photons, we exploit a phenomenon called spontaneous parametric down-conversion (SPDC) Ref. [24]. To this end, we place a pair of barium borate (BBO) crystals (both Type I, cut at a phase matching angle  $\theta = 29.2^\circ$ , with dimensions  $6 \times 6 \times 0.1$ mm, optically contacted on and each one rotated  $90^\circ$  with respect to the other) in the light path. Upon interaction with the BBO crystals, an initial single photon, called pump, can generate two down-converted (and thus, less energetic) photons. Although the probability of this process is low, one in a million, the high photon flux that reaches the BBO crystal ensures repeatable generation of Bell states.

The plane formed by the optical axis of the BBO crystal and the direction of propagation of the incident pump photon is known as the SPDC plane. Only a pump photon with polarization contained in the SPDC plane can experience SPDC and generate two photons. In this case, both photons feature a perpendicular polarization with respect to that of the incident pump photon. Instead, if the polarization of the pump photon is perpendicular to the BBO plane, the BBO crystal does not produce pairs of photons [25]. With this consideration, by illuminating the first (second) BBO crystal with horizontal (vertical) light, pairs of photons can be produced, both with vertical (horizontal) polarization, as shown in Fig. 5. The green and red cones are the  $V$ -polarized and  $H$ -polarized light cones, respectively.

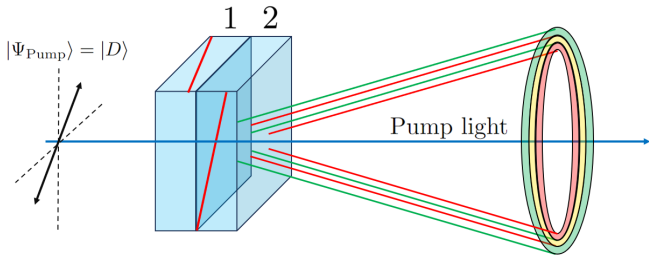


FIG. 5. Scheme of the production of entangled photons using two Type-I BBO crystals. The optical axes of the crystals represented as red line are forming  $90^\circ$ .

As the photons produced in the first BBO crystal have extraordinary polarization in the second BBO crystal, then, a relative phase  $\phi_{\text{BBO}}$  appears between the pair of photons produced in the first and the second crystal.

$$|H\rangle_{\text{Pump}} \xrightarrow{\text{BBO}'_s} |V\rangle_s \otimes |V\rangle_i, \quad (16)$$

$$|V\rangle_{\text{Pump}} \xrightarrow{\text{BBO}'_s} e^{i\phi_{\text{BBO}}} \cdot |H\rangle_s \otimes |H\rangle_i. \quad (17)$$

In our experiments, we shine the BBO crystals with a diagonally-polarized light, that is, light in an equally superposition between the  $|H\rangle$  and  $|V\rangle$  states. These photons can be down-converted in both crystals. Thus, in the region of space where both light cones overlap (yellow region in Fig. 5) the photons that we receive are indistinguishable, i.e. we cannot tell in which BBO crystal they were generated. What we do know is that, if we measure the polarization of one of them, the polarization of the other is the same. It is precisely this indistinguishability between two-photon paths gives rise to the entanglement.

Let us consider the pair of BBO crystals with their optical axes pointing in the vertical and horizontal direction. When one pump photon in the state Eq. (15) goes through them and suffers SPDC, following Eqs. (16) and (17) produces

$$|\Psi_{\text{EPR}}\rangle = \frac{1}{\sqrt{2}} \left( |VV\rangle + e^{i(\phi(\varphi) + \phi_{\text{BBO}})} |HH\rangle \right). \quad (18)$$

Changing the tilt angle  $\varphi$  of the HWP<sup>(2)</sup> we can control the relative phase between  $|VV\rangle$  and  $|HH\rangle$  components. Let us call  $\varphi^+$  and  $\varphi^-$  the angles for which we obtain

$$\begin{cases} \varphi = \varphi^+ & \rightarrow e^{i(\phi(\varphi) + \phi_{\text{BBO}})} = 1 \\ \varphi = \varphi^- & \rightarrow e^{i(\phi(\varphi) + \phi_{\text{BBO}})} = -1. \end{cases} \quad (19)$$

Finally, the four Bell states can be produced with this setup by adding a HWP. In particular, a HWP (HWP<sup>(s)</sup>) placed in the optical path corresponding to the signal photons, enables obtaining all four Bell states. As shown in Table III A, these states depend on the angles  $\varphi$  and  $\theta_s$ , where  $\theta_s$  is the angle that forms the fast axis of the HWP<sup>(s)</sup> with respect to the horizontal direction.

Bell State	Angle $\theta_s$	Angle $\varphi$
$ \Phi^+\rangle = \frac{1}{\sqrt{2}} ( HH\rangle +  VV\rangle)$	$0^\circ$	$\varphi = \varphi^+$
$ \Phi^-\rangle = \frac{1}{\sqrt{2}} ( HH\rangle -  VV\rangle)$	$0^\circ$	$\varphi = \varphi^-$
$ \Psi^+\rangle = \frac{1}{\sqrt{2}} ( HV\rangle +  VH\rangle)$	$45^\circ$	$\varphi = \varphi^+$
$ \Psi^-\rangle = \frac{1}{\sqrt{2}} ( HV\rangle -  VH\rangle)$	$45^\circ$	$\varphi = \varphi^-$

TABLE I. Value of the variables  $\varphi$  and  $\theta_s$  for the production of all four Bell States.

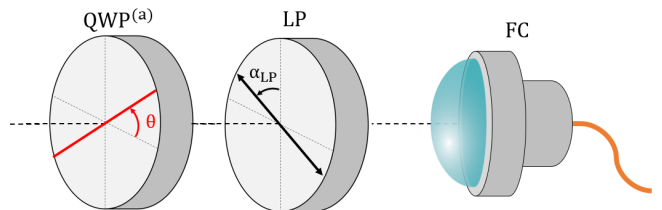


FIG. 6. Measurement scheme in the signal photons' arm in Setup 1. Photons travel from left to right, first passing through the QWP with its fast axis (red line) set at an angle  $\theta$  with respect to the horizontal. They then go through the linear polarizer, oriented at an angle  $\alpha_{\text{LP}}$  relative to the vertical. In the idler photons' arm, the scheme is the same.

## B. Photon detection

The key distinction between both setups lies in the photon detection part. In particular, in the following three aspects: 1) the number of detector channels employed, 2) the way we perform unitary transformations on the photon individually and, 3) the way the polarization is measured.

The state of one photon can be expressed in any of the basis introduced previously,

$$\begin{aligned} |\Psi\rangle &= C_V |V\rangle + C_H |H\rangle \\ &= C_{V_\alpha} |V_\alpha\rangle + C_{H_\alpha} |H_\alpha\rangle \\ &= C_R |R\rangle + C_L |L\rangle, \end{aligned} \quad (20)$$

where  $C_i$  are complex numbers. The squared modulus of these coefficients represents the probability of finding the photon in that state. Our main objective is to measure the number of photons that reach our detectors in each state of a given basis. However, we are limited in the information that we can gather. For example, by varying the polarizer angle  $\alpha$  with respect to the vertical direction in the setup shown in Fig. 3, we are restricted to measure the states located on the equator of the Bloch sphere  $\{|V_\alpha\rangle, |H_\alpha\rangle\}$  (Fig. 1 a). The setup depicted in Fig. 4 is even more restrictive, allowing access to only the basis  $\{|V\rangle, |H\rangle\}$ . To measure photons in the various bases of interest in each setup, which is needed for the Bell test and quantum state tomography experiments, retarder plates are required. A brief guideline on how to use them is presented in the following subsections.

### 1. Measurements in setup 1

In this case, the way we have to measure the photons polarization is by using first a QWP and then a linear polarizer, as depicted in Fig. 6. If we place the QWP at  $\theta = \alpha$ ,

$$\begin{aligned} \text{QWP}_{\theta=\alpha}^{(a)}(|H_\alpha\rangle) &= |H_\alpha\rangle, \\ \text{QWP}_{\theta=\alpha}^{(a)}(|V_\alpha\rangle) &= |V_\alpha\rangle, \end{aligned}$$

the QWP acts as an identity operator for the states  $|V_\alpha\rangle$  and  $|H_\alpha\rangle$ . Therefore, the QWP can be removed as it does not alter the state. Then we can measure the number of photons in the  $|V_\alpha\rangle$  and  $|H_\alpha\rangle$  states by simply placing the polarizer at an angle  $\alpha_{LP} = \alpha$  and  $\alpha_{LP} = \alpha + 90^\circ$  respectively. On the other hand, if we place the QWP at  $\theta = 45^\circ$ ,

$$\begin{aligned} \text{QWP}_{\theta=45^\circ}^{(a)}(|L\rangle) &= |H\rangle, \\ \text{QWP}_{\theta=45^\circ}^{(a)}(|R\rangle) &= |V\rangle, \end{aligned}$$

the entire  $|R\rangle$  ( $|L\rangle$ ) component of our state described in the Eq. (20) becomes  $|V\rangle$  ( $|H\rangle$ ). Therefore, if we place the polarizer at an angle  $\alpha_{LP} = 0^\circ$  ( $\alpha_{LP} = 90^\circ$ ), we obtain the same statistics as if we could measure the state of our photons before the operations with the retarder plates in the state  $|R\rangle$  ( $|L\rangle$ ). Summarizing the procedure in a table:

Angle QWP	Angle LP	Counts detected
$\alpha$	$\alpha$	$N_{ V_\alpha\rangle}$
$\alpha$	$\alpha + 90^\circ$	$N_{ H_\alpha\rangle}$
$45^\circ$	$0^\circ$	$N_{ R\rangle}$
$45^\circ$	$90^\circ$	$N_{ L\rangle}$

TABLE II. Value of the angles of the QWP and the linear polarizer for obtaining all different photon-state statistics using the setup depicted in Fig. 3.

### 2. Measurements in setup 2

In the second setup, we measure the photons polarization using first a QWP, then a HWP and finally a polarizing beam splitter (PBS), as depicted in Fig. 7. Thus, photons with vertical (horizontal) polarization are collected by the fiber-coupling lens placed in the reflected (transmitted) path of the PBS. If we place the QWP at  $\theta = \alpha$  and the HWP at  $\theta = \frac{\alpha}{2}$ , we have

$$\begin{aligned} \text{HWP}_{\theta=\frac{\alpha}{2}}^{(a)}(\text{QWP}_{\theta=\alpha}^{(a)}(|H_\alpha\rangle)) &= \text{HWP}_{\theta=\frac{\alpha}{2}}^{(a)}(|H_\alpha\rangle) = |H\rangle, \\ \text{HWP}_{\theta=\frac{\alpha}{2}}^{(a)}(\text{QWP}_{\theta=\alpha}^{(a)}(|V_\alpha\rangle)) &= \text{HWP}_{\theta=\frac{\alpha}{2}}^{(a)}(|V_\alpha\rangle) = |V\rangle, \end{aligned}$$

where the  $|V_\alpha\rangle$  and  $|H_\alpha\rangle$  components of any arbitrary state described in the eq. (20) are transformed into

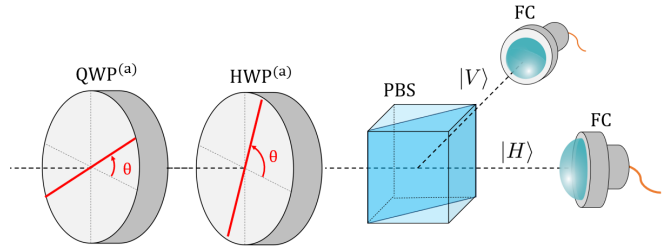


FIG. 7. Measurement scheme in the signal photons' arm in Setup 2. Photons travel from left to right, first passing through the QWP and HWP before going through the polarizing beam splitter (PBS). In the PBS, photons with vertical polarization get reflected and photons with horizontal polarization gets transmitted.

Angle QWP	Angle HWP	Counts detected in the reflected (transmitted) path
$\alpha$	$\alpha/2$	$N_{ V_\alpha\rangle}$ ( $N_{ H_\alpha\rangle}$ )
$45^\circ$	$0^\circ$	$N_{ R\rangle}$ ( $N_{ L\rangle}$ )

TABLE III. Value of the angles of the QWP and the HWP for obtaining all different photon-state statistics in the reflected and transmitted path of the PBS, using the setup depicted in Fig. 4.

$|V\rangle$  and  $|H\rangle$  components respectively. When this photons goes through the PBS, in the reflected (transmitted) path, the vertically (horizontally) polarized photons follows the same statistics as the photons in the state  $|V_\alpha\rangle$  ( $|H_\alpha\rangle$ ) before the retarder plates. On the other hand, if we place the QWP at  $\theta = 45^\circ$  and the HWP at  $\theta = 0^\circ$ , we have

$$\begin{aligned} \text{HWP}_{\theta=0^\circ}^{(a)}(\text{QWP}_{\theta=45^\circ}^{(a)}(|L\rangle)) &= \text{HWP}_{\theta=0^\circ}^{(a)}(|H\rangle) = |H\rangle, \\ \text{HWP}_{\theta=0^\circ}^{(a)}(\text{QWP}_{\theta=45^\circ}^{(a)}(|R\rangle)) &= \text{HWP}_{\theta=0^\circ}^{(a)}(|V\rangle) = |V\rangle, \end{aligned}$$

the entire  $|R\rangle$  ( $|L\rangle$ ) component of our state becomes  $|V\rangle$  ( $|H\rangle$ ). Therefore, in the reflected (transmitted) path of the PBS, the photons follows the same counting statistics as if we will be able to measure the photons in the states  $|R\rangle$  and  $|L\rangle$  respectively, before the operations with the retarder plates. Summarizing the procedure in a table:

## IV. ALIGNMENT OF THE SETUP

In this section we explain in full detail how to align our experimental setup.

### A. Alignment of the pump laser and detectors

The first thing to check once we have all the elements assembled is whether the pump laser travels parallel to

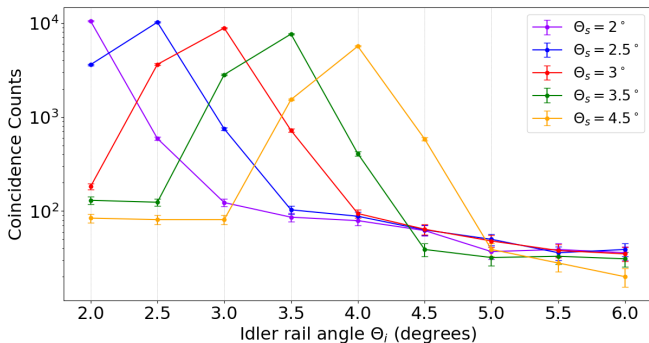


FIG. 8. Coincidence counts and averaged accidental counts for different angular positions of the metallic rails. Each of the measurements takes 30 seconds.

the optical table and through the center of the setup. To do this, we rely on the precision mounts (KS1, ThorLabs) of the two mirrors on which the pump beam is reflected.

Subsequently, we need to verify that the fiber-coupling lenses (F810FC-780, ThorLabs) are capturing photons from the BBO crystals. For this purpose, we introduce light through the other output of the optical fiber and ensure that all the light spots generated by the fiber-coupling lenses points at the BBO crystals using the precision mount (KS1, ThorLabs) in which the fiber-coupling lenses are fixed. Once this is done, we know that the lenses are collecting photons from the BBO crystals.

### B. Optimal position for the rail angles

To increase the number of collected photons, we need to find the optimal angles of the detectors rails (and therefore the fiber-coupler lenses) for which we detect the maximum number of coincident counts. We know that we are indeed detecting coincident counts from the BBO crystals when these counts deviate at least an order of magnitude from the counts that would be expected by mere chance, known as the accidental counts ( $N_{acc}$ ). These accidental counts depend on the number of counts detected individually by each of the detectors ( $N_a$  and  $N_b$ ), as well as the measurement duration ( $T$ ) and the coincidence window ( $\tau$ ), according to the following equation

$$N_{acc} = \frac{N_a \cdot N_b \cdot \tau}{T}. \quad (21)$$

In our case, the value for the coincidence window is fixed an equal to 90ns. To find the optimal position of the rails, we conduct a study in which, for a certain angle of the signal rail ( $\Theta_s$ ), we record the number of detected coincidences for various positions of the idler rail ( $\Theta_i$ ).

In Fig. 8, we find the maximum number of coincidence counts for each case when one detector is approximately at the same angle of the other detector. In particular, we find the maximum number of coincidence counts when

both detectors are between  $2^\circ$  and  $2.5^\circ$ . For mechanical reasons, when assembling all the necessary elements to take measurements on the metal rails, we cannot position both detectors at less than  $2.5^\circ$ . Therefore, from now on, in the remaining measurements, both detectors will be fixed at an angle  $\Theta_s = \Theta_i = 2.5^\circ$  with respect to the pump laser beam. At these angles, the number of coincidence counts differs by at least two orders of magnitude compared to the number of accidental counts. This indicates that the coincidence counts we detect come from photon pairs produced in the BBO crystals. It is also worth mentioning that the number of dark counts of our detector is around 350 counts per channel per second.

### C. Optimal position of the BBO crystals. Finding the direction of the optical axes

In general we do not know a priori the direction of the optical axes inside each BBO crystal. We know that a BBO crystal only produces photons when the polarization of the light is contained in the SPDC plane of the crystal [25]. In our case one BBO crystal is rotated  $90^\circ$  with respect to the other. Thus, if we shine the BBO crystals with pump light horizontally polarized and fix them inside a rotation mount (KS1RS, ThorLabs), that allows us to rotate both crystals simultaneously, we expect to find four angles in which we only detect photons in the state  $|VV\rangle$ . This occurs because, at these angles, one BBO crystal aligns its SPDC plane parallel to the pump light polarization, generating photon pairs in the state  $|VV\rangle$  while the other crystal aligns its SPDC plane perpendicular to the pump light polarization, ceasing photon production.

Then, we rotate the BBO crystals in steps of  $10^\circ$  and for each angle we measure the photons in the states  $|VV\rangle$ ,  $|VH\rangle$ ,  $|HV\rangle$  and  $|HH\rangle$ , obtaining the dependence shown in Fig. 9.

The maximal signal of photons in the  $|VV\rangle$  state is found for angles  $45^\circ$ ,  $135^\circ$ ,  $225^\circ$  and  $315^\circ$ , see Fig. 9. These are the optimal angles for the production of entangled photons when we shine the crystals with diagonally-polarized light, as one of the crystals have the optical axis pointing in the  $|H\rangle$  direction and the other in the  $|V\rangle$  direction.

### D. Finding the optimal phase matching angle

Once we have the optical axes of the BBO crystals pointing in the  $|V\rangle$  and  $|H\rangle$  directions, we illuminate them again with diagonally polarized pump light.

Our BBO crystals are cut at a phase-matching angle of  $29.2^\circ$ . That means that the optical axis of the crystal forms  $29.2^\circ$  with respect to the direction of the pump photons. This angle is not optimized for the wavelength that we are working with (405nm) [26]. However, using the precision mount in which the crystals are placed



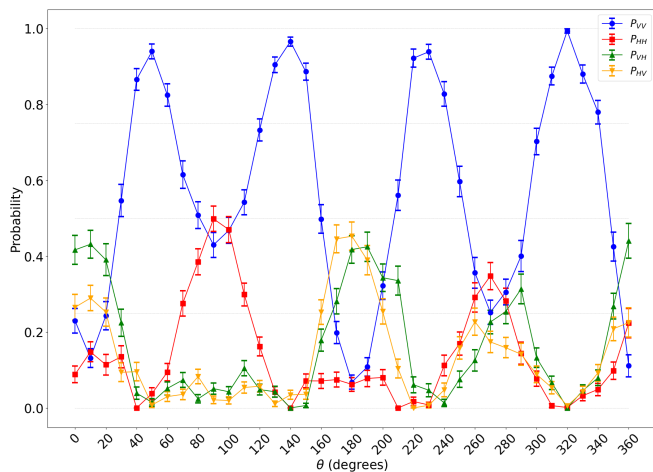


FIG. 9. Coincidence probabilities measured for various BBO crystal angles and photon-pair states. Each measurement lasts 30 seconds.

(KS1RS, ThorLabs), we can slightly tune the angle that forms the axis of each BBO crystal with respect to the pump light. This optimizes the production of photon pairs, as it offers three precision screws, arranged in an “L” shape. With the screw at the upper end, we change the phase-matching angle of the crystal whose optical axis is pointing in the vertical direction. The screw at the lower end allows us to vary the phase-matching angle of the crystal whose optical axis is pointing in the horizontal direction.

As we vary the phase-matching angle of the crystal whose optical axis is pointing in the vertical (horizontal) direction, we measure the photons reaching the detectors in the  $|HH\rangle$  ( $|VV\rangle$ ) states. This is done until we find the optimal phase-matching angle, i.e., the angle for which the highest number of photons is detected.

### E. Finding the relative phase-shift dependence with the tilt angle of the HWP<sup>(2)</sup>

The HWP<sup>(2)</sup> has its fast axis pointing in the  $|H\rangle$  direction, but is placed in a mount that allows to tilt this retarder plate around an axis perpendicular to the optical table (RP01/M, ThorLabs). This permits us to adjust the relative phase between the  $|VV\rangle$  and the  $|HH\rangle$  photons produced in the BBO crystals, as is described in Eq. (18).

If we measure the photons produced by the crystals in the state  $|D\rangle_s \otimes |D\rangle_i$  while we vary the tilt angle  $\varphi$  of the HWP<sup>(2)</sup>, we expect to find the number of coincident counts following the dependence

$$\begin{aligned} N_{|DD\rangle}(\varphi) &\propto |\langle DD|\Psi_{\text{EPR}}\rangle|^2 \\ &\propto \frac{1}{4} \cdot (1 + \cos \phi'), \end{aligned} \quad (22)$$

where  $|\Psi_{\text{EPR}}\rangle$  is the state defined in Eq. (18) and  $\phi' =$

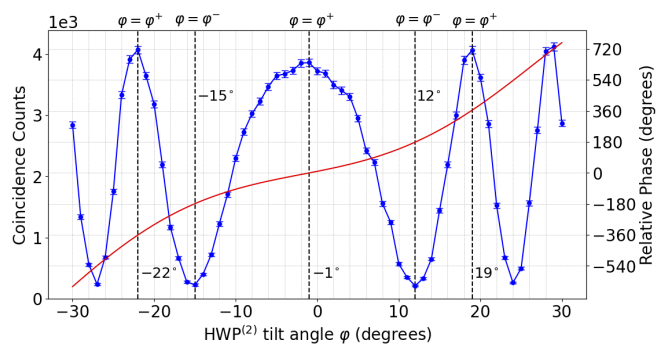


FIG. 10. The dependence of coincidence counts, represented by blue dots, and relative phase shift, depicted as a red solid line, on the tilt angle  $\varphi$  of the HWP<sup>(2)</sup>

$\phi(\varphi) + \phi_{\text{BBO}}$ . When  $\varphi = \varphi^+ + 2\pi n$  ( $\varphi = \varphi^- + 2\pi n$ ), with  $n \in \mathbb{Z}$  we expect to find a maximum (minimum) in the number of pairs of photons in the state  $|DD\rangle$  [25].

This dependence of the number of coincidence counts in the state  $|DD\rangle$  with the tilt angle  $\varphi$  can be seen in Fig. 10. For angles  $\varphi = -22^\circ$ ,  $-1^\circ$  and  $19^\circ$ , the relative phase between components is equal to  $\phi' = -2\pi$ , 0 and  $2\pi$  while for  $\varphi = -15^\circ$  and  $12^\circ$ , the relative phase between components is equal to  $\phi' = -\pi$  and  $\pi$ .

## V. ENTANGLEMENT CHARACTERIZATION, QST AND BELL TEST

Once we have the setup optimally aligned, we can characterize and perform a Bell test in all four Bell states. As explained above, the evaluation of the CHSH inequality requires measuring several correlation functions, Eq. (12), which contain coincidence probabilities among the detectors. Thus, to start characterizing the correlations arising in our detectors we compare quantum mechanical predictions to our data for a couple such correlations.

In particular, we generate the plots  $C(0^\circ, \theta)$  and  $C(45^\circ, \theta)$  to observe if the experimental results follows the results predicted by quantum mechanics. The  $C(0^\circ, \theta)$  and  $C(45^\circ, \theta)$  plots shown in Fig. 11 and 12 are obtained measuring the coincidence counts of pairs of photons in the state  $|V_{0^\circ}\rangle \otimes |V_\theta\rangle$  or  $|V_{45^\circ}\rangle \otimes |V_\theta\rangle$  respectively, while varying the angle  $\theta$  at which we measure the state of the second photon from  $0^\circ$  to  $180^\circ$  in steps of  $10^\circ$ .

Then, we also conduct quantum state tomography for each case and determine the fidelity between our state and the desired state, see Table IV. The results are shown in Fig. 11 and 12, where the Real Part and Imaginary Part in the diagrams refer to the weights of the real and imaginary parts, respectively, in the density matrix associated with the state of our photons. The coefficient associated with each of these weights can be determined by observing the labels on the axes of the diagrams.

Finally, to prove that we have indeed an entangled state, we perform the Bell test. For each of the states, we obtain a violation of the Bell inequalities with at least 40 standard deviations from the maximum classical value of  $|\langle S \rangle| = 2$ , see Table IV. As each measurement takes 30 seconds, the time needed for conducting a Bell test using Setup 1 is 20 minutes and 5 minutes with Setup 2. The resulting value for the state  $|\Phi^+\rangle$  is  $\langle S \rangle = 2.730 \pm 0.015$ .

For the tomography and the calculation of the fidelity, we use only the number of coincidence counts, while for obtaining the value of the Bell inequality, we use

the difference between coincidence counts and accidental counts, as described in Sec. D.

State	$\langle S \rangle$	$\langle S' \rangle$	Fidelity
$ \Phi^+\rangle$	$2.765 \pm 0.018$	$0.022 \pm 0.018$	$0.945 \pm 0.005$
$ \Phi^-\rangle$	$0.101 \pm 0.016$	$2.745 \pm 0.016$	$0.918 \pm 0.005$
$ \Psi^+\rangle$	$-0.055 \pm 0.019$	$-2.806 \pm 0.019$	$0.881 \pm 0.005$
$ \Psi^-\rangle$	$-2.804 \pm 0.018$	$-0.053 \pm 0.018$	$0.954 \pm 0.005$

TABLE IV. Bell test and fidelity results for each of states.

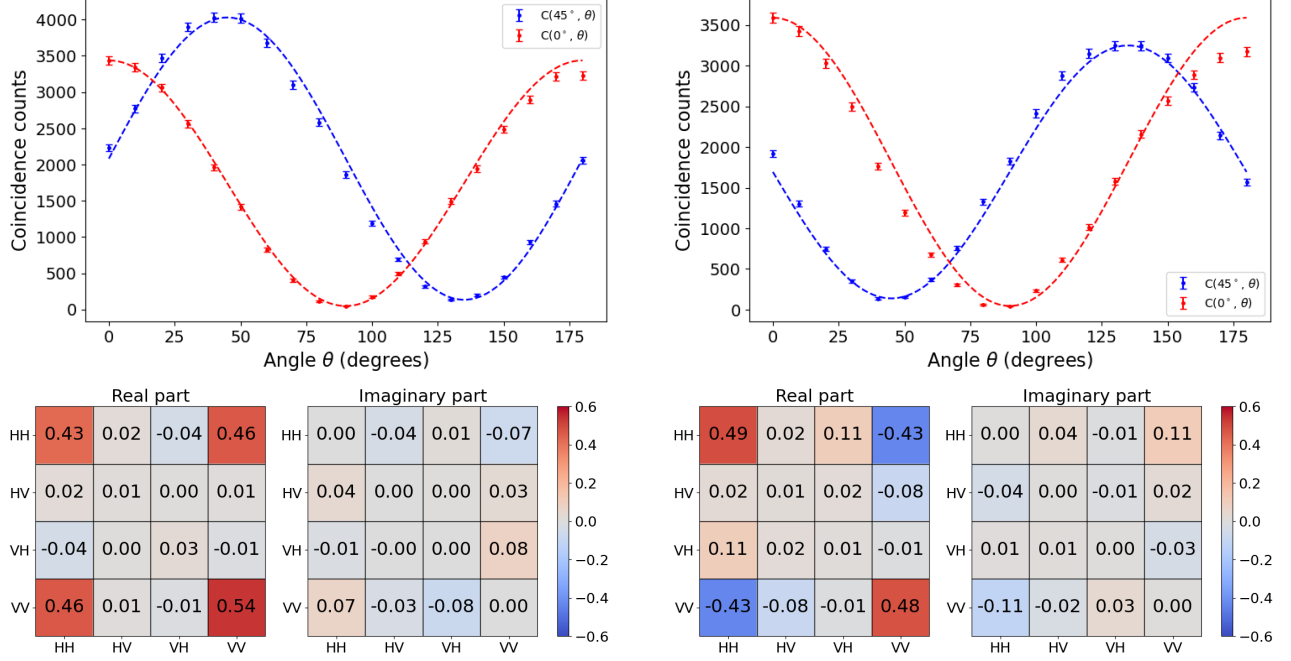


FIG. 11.  $C(0^\circ, \theta)$ ,  $C(45^\circ, \theta)$  graphs and tomography for the states  $|\Phi^+\rangle$  (left) and  $|\Phi^-\rangle$  (right). The dashed lines correspond to the quantum mechanics predictions,  $C(\theta_1, \theta_2) \propto \cos^2(\theta_1 - \theta_2)$  and  $C(\theta_1, \theta_2) \propto \cos^2(\theta_1 + \theta_2)$ , for  $|\Phi^+\rangle$  and  $|\Phi^-\rangle$ , respectively. See Sec. C.

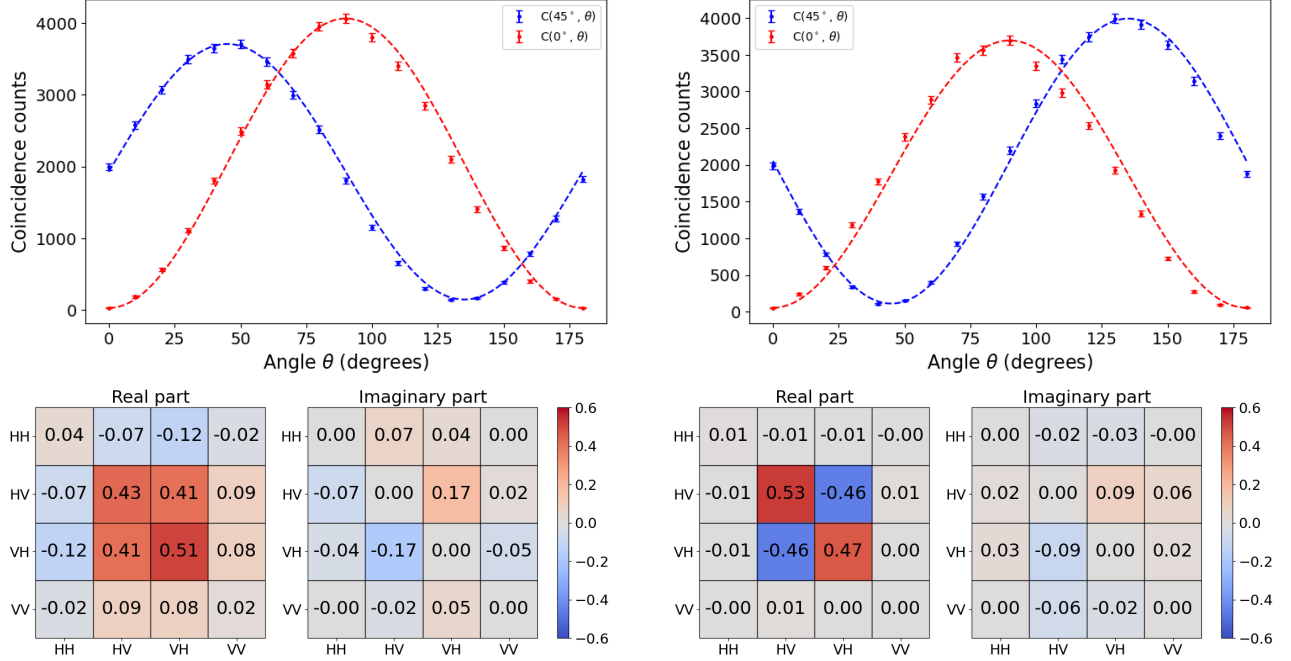


FIG. 12.  $C(0^\circ, \theta)$ ,  $C(45^\circ, \theta)$  graphs and tomography for the states  $|\Psi^+\rangle$  (left) and  $|\Psi^-\rangle$  (right). The dashed lines correspond to the quantum mechanics predictions,  $C(\theta_1, \theta_2) \propto \sin^2(\theta_1 + \theta_2)$  and  $C(\theta_1, \theta_2) \propto \sin^2(\theta_1 - \theta_2)$ , for  $|\Psi^+\rangle$  and  $|\Psi^-\rangle$ , respectively. See Sec. C.

## VI. CONCLUSIONS

We have presented a new experimental laboratory aimed at the undergraduate and master level to study quantum entangled photons. Two different setups have been described, which differ on the photon detection part. The photon production is in both cases through two BBO crystals. The photon detection is either performed with two single photon detectors or with four, allowing in the latter case to reduce the measurement time by a factor four.

The photons are collected by means of optical fibers mounted on custom made rails, thus ensuring an easy and robust alignment. The procedure to assemble and align the system from scratch, which has proven key in our experience, has been presented, thus providing a direct guide to future undergrad students in quantum science and technology laboratories worldwide.

The experiments which can be conducted are manifold. First, one can produce any of the well know Bell states, in our case produced with a fidelity higher than 88%. The full tomography of the states can be performed, thus confirming that the desired two-photon quantum state has been produced. Besides, one can also perform correlated measurements within the two photons, which can be directly confronted with quantum mechanical predictions.

Bell tests tailored for the different Bell states can also be performed. In our case, we measured violations of the corresponding inequalities by more than 40 standard deviations. With this setup, after alignment, a Bell test can be conducted in less than an hour.

All of this, combined with the fact that the total cost of components required to assemble both setups is approximately twenty thousand euros (see Sec. A), makes this experiment accessible to laboratories with limited resources. It also brings these type of demonstrations closer to undergraduate students, high school students, or even a broader audience. This facilitates the dissemination of key concepts in quantum mechanics beyond universities and specialized research groups.

## ACKNOWLEDGMENTS

We thank Marti Pedemonte and Alejandro Jaramillo for their contribution to early versions of the current setup, Morgan Mitchell for his support and suggestions over the years. We acknowledge useful and constructive discussions with Radek Lapkiewicz, Lluís Garrido and Hector Briongos. This study was supported by MCIN with funding from European Union NextGenerationEU(PRTR-C17.I1) and by Generalitat de Catalunya. We acknowledge funding from Grant No. PID2020-114626GB-I00 by MCIN/AEI/10.13039/5011 00011033 and "Unit of Excellence María de Maeztu 2020-2023" award to the Institute of Cosmos Sciences, Grant CEX2019-000918-M by MCIN/AEI/10.13039/501100011033, and Grants 2021SGR01095, 2021SGR00242 and 2021SGR01108 by Generalitat de Catalunya, and Grant 101002460-DEEP by European Research Council. This project has received funding from the European Union's Digital Europe Programme under grant agreement no. 101084035.

- 
- [1] A. Acín, I. Bloch, H. Buhrman, T. Calarco, C. Eichler, J. Eisert, D. Esteve, N. Gisin, S. J. Glaser, F. Jelezko, et al., *New Journal of Physics* **20**, 080201 (2018), URL <https://dx.doi.org/10.1088/1367-2630/aad1ea>.
  - [2] P. Shor, in *Proceedings 35th Annual Symposium on Foundations of Computer Science* (1994), pp. 124–134.
  - [3] D. Ganapathy, W. Jia, M. Nakano, V. Xu, N. Aritomi, T. Cullen, N. Kijbunchoo, S. E. Dwyer, A. Mullavey, L. McCuller, et al. (LIGO O4 Detector Collaboration), *Phys. Rev. X* **13**, 041021 (2023), URL <https://link.aps.org/doi/10.1103/PhysRevX.13.041021>.
  - [4] A. K. Ekert, *Phys. Rev. Lett.* **67**, 661 (1991), URL <https://link.aps.org/doi/10.1103/PhysRevLett.67.661>.
  - [5] A. Einstein, B. Podolsky, and N. Rosen, *Physical review* **47**, 777 (1935), URL <https://journals.aps.org/pr/abstract/10.1103/PhysRev.47.777>.
  - [6] J. S. Bell, *Physics Physique Fizika* **1**, 195 (1964), URL <https://journals.aps.org/ppf/abstract/10.1103/PhysicsPhysiqueFizika.1.195>.
  - [7] S. J. Freedman and J. F. Clauser, *Physical Review Letters* **28**, 938 (1972), URL <https://journals.aps.org/prl/abstract/10.1103/PhysRevLett.28.938>.
  - [8] A. Aspect, P. Grangier, and G. Roger, *Physical review letters* **49**, 91 (1982), URL <https://journals.aps.org/prl/abstract/10.1103/PhysRevLett.49.91>.
  - [9] M. A. Rowe, D. Kielpinski, V. Meyer, C. A. Sackett, W. M. Itano, C. Monroe, and D. J. Wineland, *Nature* **409**, 791 (2001), URL <https://www.nature.com/articles/35057215>.
  - [10] B. Hensen, H. Bernien, A. E. Dréau, A. Reiserer, N. Kalb, M. S. Blok, J. Ruitenber, R. F. Vermeulen, R. N. Schouten, C. Abellán, et al., *Nature* **526**, 682 (2015), URL <https://www-nature-com.sire.ub.edu/articles/nature15759>.
  - [11] *The nobel prize in physics 2022* (2022), URL <https://www.nobelprize.org/prizes/physics/2022/summary/>.
  - [12] E. J. Galvez, C. H. Holbrow, M. Pysher, J. Martin, N. Courtemanche, L. Heilig, and J. Spencer, *American Journal of Physics* **73**, 127 (2005), URL <https://pubs.aip.org/aapt/ajp/article-abstract/73/2/127/1040988/interference-with-correlated-photons-Five-quantum?redirectedFrom=fulltext>.
  - [13] J. Thorn, M. Neel, V. Donato, G. Bergreen, R. Davies, and M. Beck, *American journal of physics* **72**, 1210 (2004), URL <https://pubs.aip.org/aapt/ajp/article-abstract/72/9/1210/532598/>

- [Observing-the-quantum-behavior-of-light-in-an-redirectedFrom=fulltext.](#)
- [14] A. Bista, B. Sharma, and E. J. Galvez, American Journal of Physics **89**, 111 (2021), URL <https://pubs.aip.org/aapt/ajp/article-abstract/89/1/111/1045756/A-demonstration-of-quantum-key-distribution-with?redirectedFrom=fulltext>.
- [15] E. J. Galvez and M. Beck, in *Proc. SPIE* (2007), vol. 9665, p. 966513, URL <https://www.spiedigitallibrary.org/conference-proceedings-of-spie/9665/966513/Quantum-optics-experiments-with-single-photons-for-graduate-laboratories>, URL [https://doi.org/10.1117/12.2207351.full#\\_=\\_](https://doi.org/10.1117/12.2207351.full#_=_).
- [16] D. Branning, S. Bhandari, and M. Beck, American Journal of Physics **77**, 667 (2009), URL <https://pubs.aip.org/aapt/ajp/article-abstract/77/7/667/1057717/Low-cost-coincidence-counting-electronics-for?redirectedFrom=fulltext>.
- [17] B. J. Pearson and D. P. Jackson, American Journal of Physics **78**, 471 (2010), URL <https://pubs.aip.org/aapt/ajp/article-abstract/78/5/471/1040050/A-hands-on-introduction-to-single-photons-and?redirectedFrom=fulltext>.
- [18] V. Borish and H. J. Lewandowski, Phys. Rev. Phys. Educ. Res. **19**, 010117 (2023), URL <https://link.aps.org/doi/10.1103/PhysRevPhysEducRes.19.010117>.
- [19] S. G. Lukishova, Optical Engineering **61**, 081811 (2022), URL <https://opg.optica.org/abstract.cfm?uri=ETOP-2021-W2B.3>.
- [20] J. F. Clauser, M. A. Horne, A. Shimony, and R. A. Holt, Physical review letters **23**, 880 (1969), URL <https://journals.aps.org/prl/abstract/10.1103/PhysRevLett.23.880>.
- [21] M. H. Waseem, M. S. Anwar, et al., *Quantum Mechanics in the Single Photon Laboratory* (IOP Publishing, 2020), URL <https://iopscience.iop.org/book/mono/978-0-7503-3063-3>.
- [22] R. Jozsa, Journal of modern optics **41**, 2315 (1994), URL <https://www.tandfonline.com/doi/abs/10.1080/09500349414552171>.
- [23] D. Dehlinger and M. Mitchell, American Journal of Physics **70**, 903 (2002), URL <https://pubs.aip.org/aapt/ajp/article-abstract/70/9/903/1055905/Entangled-photons-nonlocality-and-Bell?redirectedFrom=fulltext>.
- [24] D. Dehlinger and M. Mitchell, American Journal of Physics **70**, 898 (2002), URL <https://pubs-aip-org.sire.ub.edu/aapt/ajp/article/70/9/898/1055898/Entangled-photon-apparatus-for-the-undergraduate>.
- [25] P. G. Kwiat, E. Waks, A. G. White, I. Appelbaum, and P. H. Eberhard, Physical Review A **60**, R773 (1999), URL <https://journals.aps.org/prl/abstract/10.1103/PhysRevA.60.R773>.
- [26] W.-D. Cheng, C.-S. Lin, H. Zhang, and G.-L. Chai, The Journal of Physical Chemistry A **126**, 7787 (2022), URL <https://pubs.acs.org/doi/10.1021/acs.jpca.2c05300>.
-

### Appendix A: List of material

For any reader interested in replicating either of the two setups, here is an inventory of useful information for acquiring all the necessary elements. The total cost of all these elements amounts to around 20.000 euros.

Description of the product	Reference and Company	Price (eur.)	Quantity
Precision kinematic mount	KS1, ThorLabs	90.51	4 + 2 <sub>2</sub>
Fiber-coupling lenses	F810FC-780, ThorLabs	267.73	2 + 2 <sub>2</sub>
Goniometer	RP01/M, ThorLabs	101.24	1
Rotation Mount	RSP1X225/M, ThorLabs	141.46	4
Rotation Mount 30mm cage system	CRM1T/M, ThorLabs	87.20	1
BBO crystals mount	KS1RS, ThorLabs	250.90	1
PBS mount	KM200PM/M, ThorLabs	127.41	2 <sub>2</sub>
4-channel detector	SPCM-AQ4C, Excelitas Technologies	13456.21	1
Current and Temperature Controllers for Laser Diodes	LTC56A/M, ThorLabs	2847.77	1
Laser diode 404nm 400mW	L404P400M, ThorLabs	684.60	1
Mirrors	BB1-E02, ThorLabs	73.83	2
BBO crystals	EKSMA Optics	1540.00	1
Bandpass Filter 405nm	FBH405-10, ThorLabs	149.69	1
Bandpass Filter 800nm	FBH800-40, ThorLabs	149.69	2 + 2 <sub>2</sub>
“Infrared” Polarizers	LPNIRE100-B, ThorLabs	116.46	2 <sub>1</sub>
Quarter-wave Plate 808nm	WPQ05M-808, ThorLabs	461.09	2
Half-wave Plate 808nm	WPH05M-808, ThorLabs	461.09	2 <sub>2</sub>
Half-wave Plate 405nm	WPH05M-405, ThorLabs	461.09	2
Polarizing Beamsplitter (PBS)	PBS252, ThorLabs	235.40	2 <sub>2</sub>
Development board for the coincidence circuit	NUCLEO-F756ZG, STMicroelectronics	22.82	1

TABLE V. Detailed equipment used in the setups. The subscripts 1 and 2 denote the quantities of elements required solely for the construction of setups 1 and 2, respectively.

### Appendix B: Stokes coefficients

The general equation for each of the Stokes coefficients of Eq. (6) is

$$S_{ij} = \text{Tr}(\sigma_i \otimes \sigma_j \cdot \rho), \quad (\text{B1})$$

where  $\rho$  is the state of our pair of photons. Thus, the explicit expression for the Stokes coefficients is,

$$\begin{aligned}
S_{00} &= P_{|HH\rangle} + P_{|HV\rangle} + P_{|VH\rangle} + P_{|VV\rangle}, \\
S_{01} &= P_{|HD\rangle} - P_{|HA\rangle} + P_{|VD\rangle} - P_{|VA\rangle}, \\
S_{02} &= P_{|HL\rangle} - P_{|HR\rangle} + P_{|VL\rangle} - P_{|VR\rangle}, \\
S_{03} &= P_{|HH\rangle} - P_{|HV\rangle} + P_{|VH\rangle} - P_{|VV\rangle}, \\
S_{10} &= P_{|DH\rangle} + P_{|DV\rangle} - P_{|AH\rangle} - P_{|AV\rangle}, \\
S_{11} &= P_{|DD\rangle} - P_{|DA\rangle} - P_{|AD\rangle} + P_{|AA\rangle}, \\
S_{12} &= P_{|DL\rangle} - P_{|DR\rangle} - P_{|AL\rangle} + P_{|AR\rangle}, \\
S_{13} &= P_{|DH\rangle} - P_{|DV\rangle} - P_{|AH\rangle} + P_{|AV\rangle}, \\
S_{20} &= P_{|LH\rangle} + P_{|LV\rangle} - P_{|RH\rangle} - P_{|RV\rangle}, \\
S_{21} &= P_{|LD\rangle} - P_{|LA\rangle} - P_{|RD\rangle} + P_{|RA\rangle}, \\
S_{22} &= P_{|LL\rangle} - P_{|LR\rangle} - P_{|RL\rangle} + P_{|RR\rangle}, \\
S_{23} &= P_{|LH\rangle} - P_{|LV\rangle} - P_{|RH\rangle} + P_{|RV\rangle}, \\
S_{30} &= P_{|HH\rangle} + P_{|HV\rangle} - P_{|VH\rangle} - P_{|VV\rangle}, \\
S_{31} &= P_{|HD\rangle} - P_{|HA\rangle} - P_{|VD\rangle} + P_{|VA\rangle}, \\
S_{32} &= P_{|HL\rangle} - P_{|HR\rangle} - P_{|VL\rangle} + P_{|VR\rangle}, \\
S_{33} &= P_{|HH\rangle} - P_{|HV\rangle} - P_{|VH\rangle} + P_{|VV\rangle}.
\end{aligned}$$

**Appendix C: Computation of  $P_{|V_{\theta_1} V_{\theta_2}\rangle}$  for all four Bell States**

We define  $P_{|V_{\theta_1} V_{\theta_2}\rangle}$  as the probability of finding the two photons in the state  $|V_{\theta_1}\rangle \otimes |V_{\theta_2}\rangle$ . The values of this probabilities for each one of the states are:

- For  $|\Phi^+\rangle = \frac{1}{\sqrt{2}}(|HH\rangle + |VV\rangle)$ :

$$\begin{aligned}
 P_{|V_{\theta_1} V_{\theta_2}\rangle} &= |\langle \Phi^+ | V_{\theta_1} V_{\theta_2} \rangle|^2 \\
 &= \left| \frac{1}{\sqrt{2}} (\langle HH | + \langle VV |) \cdot (\sin \theta_1 \sin \theta_2 |HH\rangle + \cos \theta_1 \cos \theta_2 |VV\rangle - \sin \theta_1 \cos \theta_2 |HV\rangle - \cos \theta_1 \sin \theta_2 |VH\rangle) \right|^2 \\
 &= \left| \frac{1}{\sqrt{2}} (\sin \theta_1 \sin \theta_2 + \cos \theta_1 \cos \theta_2) \right|^2 = \left| \frac{1}{\sqrt{2}} \cos(\theta_1 - \theta_2) \right|^2 = \frac{1}{2} \cos^2(\theta_1 - \theta_2)
 \end{aligned} \tag{C1}$$

- For  $|\Phi^-\rangle = \frac{1}{\sqrt{2}}(|HH\rangle - |VV\rangle)$ :

$$\begin{aligned}
 P_{|V_{\theta_1} V_{\theta_2}\rangle} &= |\langle \Phi^- | V_{\theta_1} V_{\theta_2} \rangle|^2 \\
 &= \left| \frac{1}{\sqrt{2}} (\langle HH | - \langle VV |) \cdot (\sin \theta_1 \sin \theta_2 |HH\rangle + \cos \theta_1 \cos \theta_2 |VV\rangle - \sin \theta_1 \cos \theta_2 |HV\rangle - \cos \theta_1 \sin \theta_2 |VH\rangle) \right|^2 \\
 &= \left| \frac{1}{\sqrt{2}} (\sin \theta_1 \sin \theta_2 - \cos \theta_1 \cos \theta_2) \right|^2 = \left| \frac{1}{\sqrt{2}} \cos(\theta_1 + \theta_2) \right|^2 = \frac{1}{2} \cos^2(\theta_1 + \theta_2)
 \end{aligned} \tag{C2}$$

- For  $|\Psi^+\rangle = \frac{1}{\sqrt{2}}(|HV\rangle + |VH\rangle)$ :

$$\begin{aligned}
 P_{|V_{\theta_1} V_{\theta_2}\rangle} &= |\langle \Psi^+ | V_{\theta_1} V_{\theta_2} \rangle|^2 \\
 &= \left| \frac{1}{\sqrt{2}} (\langle HV | + \langle VH |) \cdot (\sin \theta_1 \sin \theta_2 |HH\rangle + \cos \theta_1 \cos \theta_2 |VV\rangle - \sin \theta_1 \cos \theta_2 |HV\rangle - \cos \theta_1 \sin \theta_2 |VH\rangle) \right|^2 \\
 &= \left| \frac{1}{\sqrt{2}} (\sin \theta_1 \cos \theta_2 + \cos \theta_1 \sin \theta_2) \right|^2 = \left| \frac{1}{\sqrt{2}} \sin(\theta_1 + \theta_2) \right|^2 = \frac{1}{2} \sin^2(\theta_1 + \theta_2)
 \end{aligned} \tag{C3}$$

- For  $|\Psi^-\rangle = \frac{1}{\sqrt{2}}(|HV\rangle - |VH\rangle)$ :

$$\begin{aligned}
 P_{|V_{\theta_1} V_{\theta_2}\rangle} &= |\langle \Psi^- | V_{\theta_1} V_{\theta_2} \rangle|^2 \\
 &= \left| \frac{1}{\sqrt{2}} (\langle HV | - \langle VH |) \cdot (\sin \theta_1 \sin \theta_2 |HH\rangle + \cos \theta_1 \cos \theta_2 |VV\rangle - \sin \theta_1 \cos \theta_2 |HV\rangle - \cos \theta_1 \sin \theta_2 |VH\rangle) \right|^2 \\
 &= \left| \frac{1}{\sqrt{2}} (\sin \theta_1 \cos \theta_2 - \cos \theta_1 \sin \theta_2) \right|^2 = \left| \frac{1}{\sqrt{2}} \sin(\theta_1 - \theta_2) \right|^2 = \frac{1}{2} \sin^2(\theta_1 - \theta_2)
 \end{aligned} \tag{C4}$$

We can summarize all this in Table VI.

Bell State	$P_{ V_{\theta_1} V_{\theta_2}\rangle}$
$ \Phi^+\rangle$	$\frac{1}{2} \cos^2(\theta_1 - \theta_2)$
$ \Phi^-\rangle$	$\frac{1}{2} \cos^2(\theta_1 + \theta_2)$
$ \Psi^+\rangle$	$\frac{1}{2} \sin^2(\theta_1 + \theta_2)$
$ \Psi^-\rangle$	$\frac{1}{2} \sin^2(\theta_1 - \theta_2)$

TABLE VI. Values of  $P_{|V_{\theta_1} V_{\theta_2}\rangle}$  for each one of the Bell states.

### Appendix D: Data for each Bell Test

In this section, we present all the data obtained for each one of the Bell test performed to the different Bell states using the setup depicted in Fig. 3. We also provide the data for the Bell test achieved with the photons in the state  $|\Phi^+\rangle$ , using the setup presented in Fig. 4. In all these graphs, the angles  $\alpha$  and  $\beta$  stands for the angles at which Alice ( $|V_\alpha\rangle$ ) and Bob ( $|V_\beta\rangle$ ) measure their respective photons. Each of these measurements was taken using a time interval of 30 seconds.

$\alpha$ ( $^\circ$ )	$\beta$ ( $^\circ$ )	$N_a$	$N_b$	$N_c$	$N_{acc}$
45	22.5	242324	126944	3025	92.28
45	-22.5	241250	125920	377	91.13
45	-67.5	244869	142160	1242	104.43
45	-112.5	250568	145332	3959	109.25
0	22.5	231257	137000	3432	95.05
0	-22.5	235528	132632	2975	93.72
0	-67.5	226909	138908	310	94.56
0	-112.5	226724	143352	1028	97.50
-45	22.5	234822	135900	763	95.74
-45	-22.5	234676	132592	3684	93.35
-45	-67.5	233508	145184	3376	101.70
-45	-112.5	229828	150008	545	103.43
-90	22.5	224928	129820	394	87.60
-90	-22.5	222538	123984	927	82.77
-90	-67.5	217928	135868	3728	88.83
-90	-112.5	223545	141888	3031	95.16

TABLE VII. Data obtained for the computation of the Bell inequality using pairs of photons in the  $|\Phi^+\rangle$ .

$\alpha$ ( $^\circ$ )	$\beta$ ( $^\circ$ )	$N_a$	$N_b$	$N_c$	$N_{acc}$
45	22.5	220634	157440	721	104.21
45	-22.5	226207	151083	3995	102.53
45	-67.5	226708	173348	4562	117.90
45	-112.5	221408	182304	1134	121.09
0	22.5	208526	157300	4001	98.40
0	-22.5	214617	149412	3915	96.20
0	-67.5	208804	169832	565	106.38
0	-112.5	213806	182984	1001	117.37
-45	22.5	245625	157568	4293	116.11
-45	-22.5	246193	149052	683	110.09
-45	-67.5	240321	168744	1417	121.66
-45	-112.5	241023	178476	4720	129.05
-90	22.5	259133	157176	852	122.19
-90	-22.5	259584	149428	835	116.37
-90	-67.5	254570	174292	4523	133.11
-90	-112.5	259205	182424	4554	141.86

TABLE VIII. Data obtained for the computation of the Bell inequality using pairs of photons in the  $|\Phi^-\rangle$  state.



$\alpha$ ( $^\circ$ )	$\beta$ ( $^\circ$ )	$N_a$	$N_b$	$N_c$	$N_{acc}$
45	22.5	202953	140256	2997	85.40
45	-22.5	209729	140292	589	88.27
45	-67.5	199521	132980	854	79.60
45	-112.5	199216	138172	3409	82.58
0	22.5	195788	135044	520	79.32
0	-22.5	191147	126572	716	72.58
0	-67.5	196727	130908	3435	77.26
0	-112.5	191245	138028	3167	79.19
-45	22.5	185983	135516	648	75.61
-45	-22.5	187608	130676	3189	73.55
-45	-67.5	188891	133528	2898	75.67
-45	-112.5	185914	136744	470	76.27
-90	22.5	179726	137788	2973	74.29
-90	-22.5	178394	131576	2709	70.42
-90	-67.5	179378	131052	401	70.52
-90	-112.5	175836	133828	642	70.60

TABLE IX. Data obtained for the computation of the Bell inequality using pairs of photons in the  $|\Psi^+\rangle$  state.

$\alpha$ ( $^\circ$ )	$\beta$ ( $^\circ$ )	$N_a$	$N_b$	$N_c$	$N_{acc}$
45	22.5	205843	152544	1026	94.20
45	-22.5	202783	146180	3625	88.93
45	-67.5	203926	136128	2977	83.28
45	-112.5	203209	140200	370	85.47
0	22.5	199956	155508	476	93.28
0	-22.5	198214	149576	728	88.94
0	-67.5	194361	139668	3686	81.44
0	-112.5	195118	143816	3027	84.18
-45	22.5	209593	155160	3400	97.56
-45	-22.5	209790	149908	643	94.35
-45	-67.5	207594	136140	740	84.79
-45	-112.5	202074	142580	3403	86.44
-90	22.5	197175	147948	3358	87.51
-90	-22.5	202596	146072	3212	88.78
-90	-67.5	204167	135736	438	83.14
-90	-112.5	202654	143952	860	87.52

TABLE X. Data obtained for the computation of the Bell inequality using pairs of photons in the  $|\Psi^-\rangle$  state.

$\alpha$ ( $^\circ$ )	$\beta$ ( $^\circ$ )	$N_a$	$N_b$	$N_c$	$N_{acc}$
45	22.5	305415	248380	5302	227.57
45	-22.5	280234	237452	1709	199.62
45	-67.5	190449	247220	859	141.24
45	-112.5	210298	247104	5626	155.89
0	22.5	305380	320864	6682	293.95
0	-22.5	288215	312288	6478	270.01
0	-67.5	194873	321212	1267	187.78
0	-112.5	201912	301124	1538	182.40
-45	22.5	294989	231004	2013	204.43
-45	-22.5	280329	230040	5343	193.46
-45	-67.5	184691	232300	4809	128.71
-45	-112.5	202687	237160	604	144.20
-90	22.5	292146	164976	729	144.59
-90	-22.5	278696	170320	513	142.40
-90	-67.5	174801	158404	4295	83.06
-90	-112.5	201492	164912	4770	99.68

TABLE XI. Data obtained for the computation of the Bell inequality with the setup depicted in Fig. 4, using pairs of photons in the  $|\Phi^+\rangle$  state.

Assuming that the counts follow a Poisson distribution, the error corresponding to the number of counts detected in a certain time interval is equal to the square root of that value. That is:

$$\sigma_{N_a} = \sqrt{N_a}, \quad (D1)$$

$$\sigma_{N_b} = \sqrt{N_b}, \quad (D2)$$

$$\sigma_{N_c} = \sqrt{N_c}. \quad (D3)$$

Therefore, performing error propagation in Eq. (21), we have that the error in  $N_{acc}$  is,

$$\sigma_{N_{acc}} = \frac{\tau}{T} \cdot \sqrt{N_b^2 \cdot \sigma_{N_a}^2 + N_a^2 \cdot \sigma_{N_b}^2} = \frac{\tau}{T} \cdot \sqrt{N_b^2 \cdot N_a + N_a^2 \cdot N_b}, \quad (D4)$$

where we have assumed that the values  $T$  and  $\tau$  have no associated error. For simplicity, we define  $N_{VV} = N_{|V_\alpha V_\beta\rangle} = N_c(|V_\alpha V_\beta\rangle) - N_{acc}(|V_\alpha V_\beta\rangle)$  as the number of detected coincidence counts minus the number of accidental coincidence counts and  $\sigma_{N_{VV}} = \sigma_N(|V_\alpha V_\beta\rangle)$  to their associated error,

$$\sigma_{N_{VV}} = \sqrt{\sigma_{N_c}^2(|V_\alpha V_\beta\rangle) + \sigma_{N_{acc}}^2(|V_\alpha V_\beta\rangle)}. \quad (D5)$$

Then, the equation for the different probabilities is

$$\begin{aligned} P_{|V_\alpha V_\beta\rangle} &= \frac{N_{|V_\alpha V_\beta\rangle}}{N_{|V_\alpha V_\beta\rangle} + N_{|V_{\alpha-90^\circ} V_\beta\rangle} + N_{|V_\alpha V_{\beta-90^\circ}\rangle} + N_{|V_{\alpha-90^\circ} V_{\beta-90^\circ}\rangle}} \\ &= \frac{N_{|V_\alpha V_\beta\rangle}}{N_{|V_\alpha V_\beta\rangle} + N_{|H_\alpha V_\beta\rangle} + N_{|V_\alpha H_\beta\rangle} + N_{|H_\alpha H_\beta\rangle}} \\ &= \frac{N_{VV}}{N_{VV} + N_{HV} + N_{VH} + N_{HH}}, \end{aligned} \quad (D6)$$

where, from the Eq. (4), we extract that  $|V_{\gamma-90^\circ}\rangle = |H_\gamma\rangle$ . The error associated to the probability  $P_{|V_\alpha V_\beta\rangle}$  can be written as

$$\sigma_{P_{|V_\alpha V_\beta\rangle}} = \frac{1}{(N_{VV} + N_{HH} + N_{VH} + N_{HH})^2} \cdot \sqrt{N_{VV}^2 \cdot (\sigma_{N_{VH}}^2 + \sigma_{N_{HV}}^2 + \sigma_{N_{HH}}^2) + (N_{HV} + N_{VH} + N_{HH})^2 \cdot \sigma_{N_{VV}}^2}. \quad (D7)$$

For the correlation functions, defined as in Eq. (12), we have that the error is

$$\sigma_{E(\alpha,\beta)} = \sqrt{\sigma_{P|V_\alpha V_\beta}^2 + \sigma_{P|V_\alpha H_\beta}^2 + \sigma_{P|H_\alpha V_\beta}^2 + \sigma_{P|H_\alpha H_\beta}^2}. \quad (\text{D8})$$

Finally, for both functions  $S$  and  $S'$ , defined in Eq. (13) and Eq. (14), we have the same associated error,

$$\sigma_S = \sigma_{S'} = \sqrt{\sigma_{E(\alpha,\beta)}^2 + \sigma_{E(\alpha,\beta')}^2 + \sigma_{E(\alpha',\beta)}^2 + \sigma_{E(\alpha',\beta')}^2}. \quad (\text{D9})$$

Also, we define the coverage ratio as the distance in standard deviations between the absolute value of our value obtained in the CHSH inequality and the maximum value that can be obtained classically, i.e. 2. Thus,

$$\begin{aligned} \text{Coverage Ratio} &= \frac{|\langle S \rangle| - 2}{\sigma_S} \quad \text{for } |\Phi^+\rangle \text{ and } |\Psi^-\rangle \\ &= \frac{|\langle S' \rangle| - 2}{\sigma_{S'}} \quad \text{for } |\Phi^-\rangle \text{ and } |\Psi^+\rangle. \end{aligned} \quad (\text{D10})$$


---